electronics

Article

A Novel Extensional Bulk Mode Resonator with Low Bias Voltages

Qianqian Jia [1,2], Zeji Chen [1,2], Wenli Liu [1,2], Jinling Yang [1,2,*], Yinfang Zhu [1,2,*] and Fuhua Yang [1,3]

1 Institute of Semiconductors, Chinese Academy of Sciences, Beijing 100083, China; jiaqianqian@semi.ac.cn (Q.J.); chenzeji@semi.ac.cn (Z.C.); liuwenli@semi.ac.cn (W.L.); fhyang@semi.ac.cn (F.Y.)
2 Center of Materials Science and Optoelectronics Engineering, University of Chinese Academy of Sciences, Beijing 100049, China
3 State Key Laboratory of Transducer Technology, Shanghai 200050, China
* Correspondence: jlyang@semi.ac.cn (J.Y.); yfzhu@semi.ac.cn (Y.Z.)

Abstract: This paper presents a novel Π-shaped bulk acoustic resonator (ΠBAR) with low bias voltages. Concave flanges were coupled with straight beams to effectively enlarge the transduction area. A silicon-on-insulator(SOI)-based fabrication process was developed to produce nanoscale spacing gaps. The tether designs were optimized to minimize the anchor loss. With a substantially improved electromechanical coupling coefficient, the high-stiffness ΠBAR can be driven into vibrations with low bias voltages down to 3 V. The resonator, vibrating at 20 MHz, implements Q values of 3600 and 4950 in air and vacuum, respectively. Strategies to further improve the resonator performance and robustness were investigated. The resonator has promising IC compatibility and could have potential for the development of high-performance timing reference devices.

Keywords: MEMS resonator; quality factor; bias voltage; fabrication methodology

check for updates

Citation: Jia, Q.; Chen, Z.; Liu, W.; Yang, J.; Zhu, Y.; Yang, F. A Novel Extensional Bulk Mode Resonator with Low Bias Voltages. *Electronics* **2022**, *11*, 910. https://doi.org/10.3390/electronics11060910

Academic Editors: Slawomir Wiak, Paolo Di Barba and Lukasz Szymanski

Received: 16 February 2022
Accepted: 14 March 2022
Published: 15 March 2022

1. Introduction

Frequency references are ubiquitous in electronic systems [1]. Fast-growing electronic systems now generate stringent requirements for frequency reference devices in terms of integration and miniaturization [2–4]. Widely used quartz crystals of large volume are off-chip devices which have limited potential for application in constituting monolithic oscillators. Recently, micro-electro-mechanical-system (MEMS) resonators have emerged as viable candidates to replace quartz crystals because of their tiny size, high frequencies, as well as promising quality factors (Q), low power consumption and integrated circuit (IC) compatibility [5–9].

Among various vibrating modes of MEMS resonators, bulk acoustic wave (BAW) modes are superior to flexural modes due to their high stiffnesses and low dissipation [10–13]. Some BAW resonators with excellent performance have been produced. However, such resonators are still difficult to excite due to their high stiffnesses, while the capacitive spacing gaps are not narrow enough to provide high electromechanical couplings. For example, a 10.3 MHz thin-plate-shaped BAW resonator vibrating in thickness-extensional mode was driven using a single-side electrostatic configuration for which the Q and bias voltage were 9000 and 50 V, respectively [14]. A Lamé-mode resonator of 12.9 MHz exhibited a high Q of 7.5×10^5; however, the relatively large spacing gap of 2 µm led to a high DC bias voltage of 100 V [15]. More recently, I-shaped bulk acoustic resonators (IBAR) with improved Q values and lower phase noise have been proposed for timing references which are more suitable to constitute temperature-compensated (TC) oscillators ranging from 1 to 30 MHz [16–21]. For instance, a 10 MHz IBAR with a promising Q exceeding 250,000 implemented a relatively low bias voltage of 25 V; nevertheless, it was still far beyond the standard voltage of CMOS circuitries [20]. Very high bias voltages are needed in reported studies which creates a bottleneck constraining high-end applications of state-of-the-art MEMS resonators.

This paper describes the development of a capacitively transduced, Π-shaped bulk acoustic resonator (ΠBAR) with low bias voltages. The resonator was optimized in terms of the structural design and fabrication process, which effectively enlarged the transduction area and reduced the spacing gap, thus enabling significantly improved electromechanical coupling coefficient. The DC bias voltage could be reduced to 3 V.

2. Design and Fabrication

When a DC bias voltage of V_{DC} and an AC signal with an amplitude of V_i are applied to a capacitive resonator, an electrostatic force is generated, according to [22]:

$$F = V_{DC} V_i \frac{\partial C}{\partial x} = V_{DC} V_i \frac{\varepsilon_0 A}{d_0^2}, \tag{1}$$

where ε_0, d_0, and A denote the permittivity, spacing gap, and transduction area, respectively.

The equivalent mass at any point can be calculated via the kinetic energy theorem as below [22,23]:

$$m_{re} = \frac{KE_{total}}{\frac{1}{2}[v_{\max}(x,y)]^2} = \frac{\frac{1}{2}\int [\omega U_{mode}(x,y)]^2 dm}{\frac{1}{2}[\omega U_{mode\_\max}(x,y)]^2} = \frac{\rho h \iint_S [U_{mode}(x,y)]^2 dS}{[U_{mode\_\max}(x,y)]^2}, \tag{2}$$

where U_{mode} (x, y) is the in-plane mode shape function with out-of-plane vibrations neglected, ω is the angular resonance frequency, S denotes the in-plane area of the Π-shaped resonator, h is the thickness of the resonator, and ρ is the density.

At resonance, the displacement X induced by the external force can be written as:

$$X = Q\frac{F}{k_{re}}, \tag{3}$$

where k_{re} refers to the equivalent stiffness, F is the electrostatic force. The motional current takes the form:

$$i = V_{DC}\frac{\partial C}{\partial t} = V_{DC}\frac{\partial C}{\partial x}\frac{\partial x}{\partial t}, \tag{4}$$

Substituting Equations (1)–(3) into Equation (4), the motional current can be written as:

$$i = V_{DC}\frac{\varepsilon_0 A}{d_0^2}X = \frac{Q V_{DC}^2 V_i A^2}{d_0^4}\frac{\varepsilon_0^2}{\rho h \omega^2}\frac{[U_{mode\_\max}(x,y)]^2}{\iint_S [U_{mode}(x,y)]^2 dS}. \tag{5}$$

Clearly, with a given excitation condition, the motional current depends on Q, d_0, and A. It can be inferred from Equation (5) that, to acquire large motional currents with low bias voltages, shrinking the spacing gap, d_0, contributes most to the bias voltage reduction owing to its quadratic dependence. Other strategies, including increasing the transduction areas and improving Q values, are also helpful. Therefore, the resonator optimizations were carried out in terms of these three routings.

The electro-mechanical coupling coefficient of ΠBAR [24] are expressed as:

$$\eta = V_{DC}\frac{\partial C}{\partial x} = V_{DC}\frac{\varepsilon_0 A}{g^2}, \tag{6}$$

The schematic and mode shape of ΠBAR is shown in Figure 1a, where two beams working in the length-extensional mode are utilized for vibrational coupling, and two large flanges are located at both ends of the beams to provide large transduction areas. Two electrodes with complementary shapes of the flanges are configured to form the capacitance plates with spacing gaps of 70 nm.

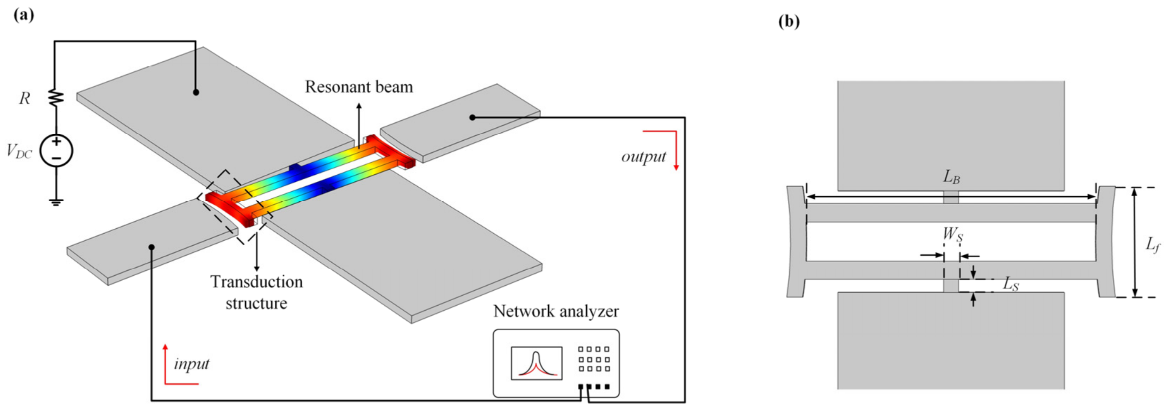

Figure 1. The schematic of ΠBAR (**a**) and illustration of the resonator structure (**b**).

2.1. Enlarged Transduction Area

From Equation (6), it can be inferred that the electro-mechanical coupling coefficient can be effectively improved by increasing transduction areas. As shown in Figure 1b, the concave flanges were employed to enlarge transduction areas while maintaining a compact resonator size. With flexible adjustments of the flange curvature, projection length and other geometrical parameters, a larger transduction area can be obtained; meanwhile, the strain energy distribution of the device can also be modified for improved Q values.

The resonance frequency is dependent on the flange shapes, which can be expressed as [25]:

$$f_0 = \frac{\alpha}{2L_B}\sqrt{\frac{E}{\rho}}, \tag{7}$$

where L_B is the length of resonant beam, E is Young's modulus, and α is a constant associated with the flange designs. In this study, three types of ΠBAR resonators were designed. Both type A and type B have straight coupling beams, while their flanges are straight and concave, respectively. To comprehensively compare the performance among ΠBAR resonators with different component shapes, the counterpart, which comprises of straight flanges and curved coupling beams, was also designed, referred as type C. The frequencies of the three types were 26.7 MHz, 20 MHz, and 26.7 MHz, corresponding to α values of 0.6936, 0.7703, and 0.8495, respectively.

2.2. Minimized Anchor Loss

The Q values of MEMS resonators can be defined as the ratio between the total stored energy and the average energy loss per cycle [12], including several dissipation mechanisms including anchor loss, air damping, surface loss, and so on [26]:

$$\frac{1}{Q_{\text{total}}} = \frac{1}{Q_{\text{anchor}}} + \frac{1}{Q_{\text{air}}} + \frac{1}{Q_{\text{surface}}} + \cdots, \tag{8}$$

The supporting loss is generally a dominant energy dissipation mechanism for BAW resonators which is associated with the energy leak from the resonator through tethers and transmits into the substrate [27]. The tethers are placed at the centers of the coupling beams, corresponding to the nodal regions of the mode shape, so that the anchor loss can be minimized. As shown in Figure 2, the anchor loss can be characterized by a finite element analysis (FEA) model in COMSOL, wherein perfectly matched layers (PML) were utilized to absorb the elastic waves propagating in the substrate [11,28]. Given that Q_{anchor} is associated with the strain energy distribution which depends on both resonator and tether designs [29,30], the geometrical parameters of the whole device were properly modified using the parametric sweeping methodology to minimize anchor loss.

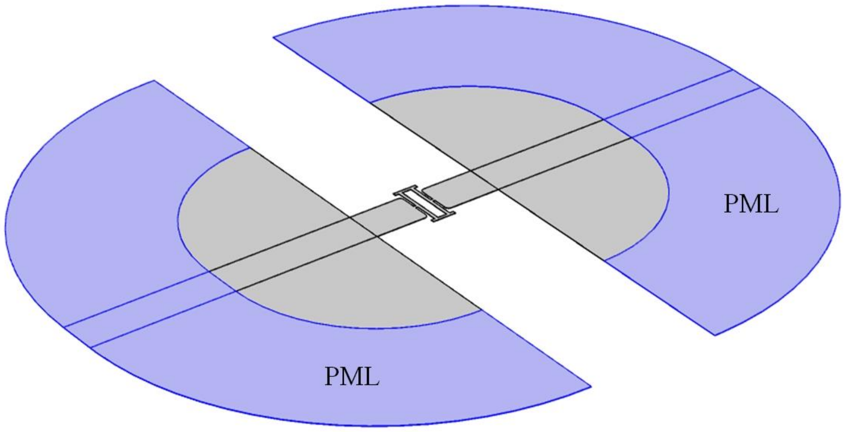

Figure 2. FEA Simulation model for Q_{anchor} values with PMLs incorporated.

2.3. Shrunk Spacing Gap

The nanoscale capacitance gap is critical for reducing the bias voltages. As illustrated in Figure 3, a simple and reliable fabrication process was used [4,31]. SOI wafers with low-resistivity single crystal silicon (SCS) device layers (Figure 3a) were employed to batch fabricate the proposed resonators. A layer of SiO_2 was grown by plasma-enhanced chemical vapor deposition (PECVD) to serve as an etching mask (Figure 3b). The resonant structure and electrical routings were defined by successive inductive-coupled-plasma (ICP) dry etching of the SiO_2 and the SCS device layer (Figure 3c). Next, a nanoscale spacing gap was defined by thermal oxidation, followed by removing the SiO_2 on the electrical routings (Figure 3d). Subsequently, polysilicon was deposited (Figure 3e) and patterned to form the electrodes. After producing the Au/Cr electrode pads using an e-beam evaporation and lift-off process, the resonators were finally released in HF solution (Figure 3f). The scanning electron microscope (SEM) photographs of the fabricated resonators are shown in Figure 4.

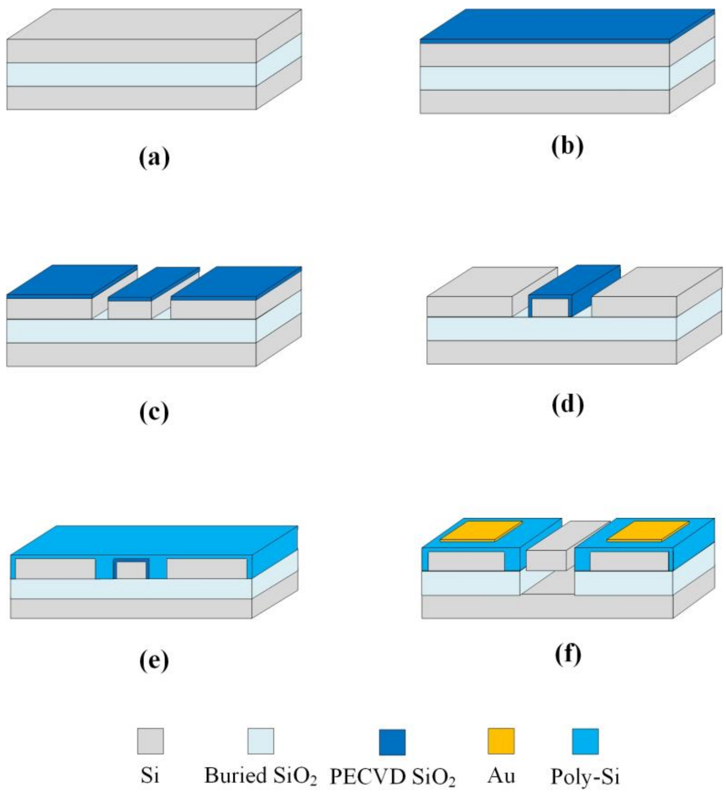

Figure 3. Process flow for the ΠBAR.

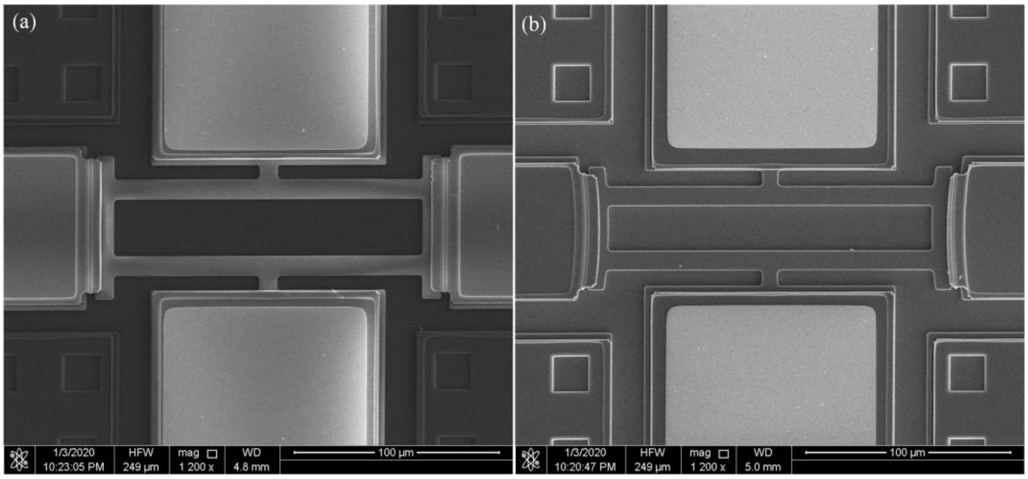

Figure 4. SEM photographs of the fabricated type A (**a**) and type B (**b**) resonators.

The test setup is shown in Figure 1a. A bias voltage V_{DC} was applied to the resonator through a U8032A voltage source, and an Agilent E5071C network analyzer was employed to apply a 0 dBm AC signal and to capture the S_{21} transmission spectra.

3. Results and Discussions

3.1. Resonator Performance

Figure 5 shows the frequency responses of various ΠBARs. As can be seen, despite the high stiffness of BAW extensional modes, the resonators can be driven into vibrations with DC bias voltages down to 3 V, owing to the enlarged transduction area as well as the nanoscale spacing gap. The Q values of the three types of ΠBARs in air were 2580, 3600, and 2340, respectively. Compared with types A and C, no significant distortions were observed in the frequency response of type B. This could have resulted from the preferable vibration transfer between the straight coupling beams and concave flanges, which suffered less from the spurious modes. In addition, concave flanges with large transduction area enabled the highest resonance peak among the three types, and hence the lowest motional resistance. The measured Q value of type A was higher than type C, however, the peak shape was asymmetrical, probably due to the fabrication tolerance which disturbed the displacement profile and increased extra energy dissipation. Warping occurred for the proposed resonator, which essentially gave rise not only to more energy dissipation, but also mode shape distortions. It was the mode distortions that gave rise to simultaneous in-plane and out-of-plane vibrations which impaired the mechanical responses of the resonator. Therefore, asymmetrical peak shapes appeared in the frequency spectra. In addition to fabrication tolerances, the curved coupling beams were detrimental to the vibrational energy transfer of type C, leading to more severe anchor loss. Thus, the S_{21} transmission spectrum was distorted, accompanied by the lowest Q. Moreover, type C had the smallest transduction area which contributed to the largest motional resistance.

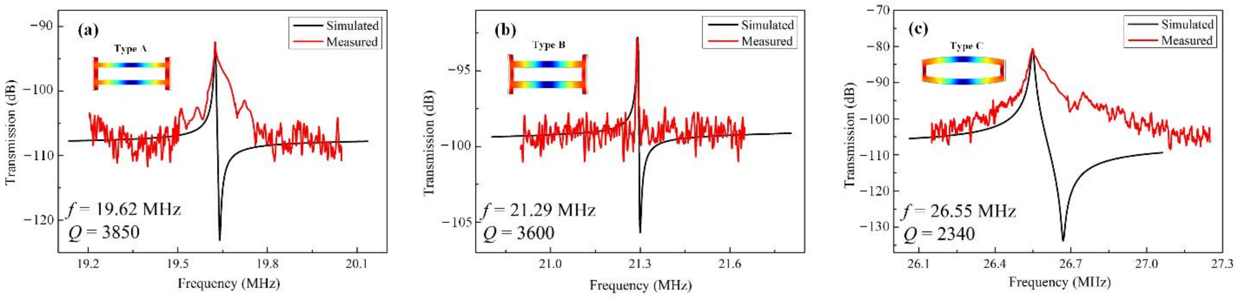

Figure 5. Frequency spectra of ΠBAR of type A (**a**), type B (**b**), and type C (**c**).

To fully analyze the electrical properties of the resonator, the equivalent circuit was established as shown in Figure 6 [29]. As can be seen, the RLC branch essentially characterizes the resonance properties of the resonator. R_m, L_m, and C_m denote the motional resistance, inductance, and capacitance, respectively, which can be described as:

$$R_m = 2Z_0\left(10^{-\left(\frac{G_{peak}}{20}\right)} - 1\right),\ L_m = \frac{QR_m}{\omega},\ C_m = \frac{1}{\omega QR_m}, \tag{9}$$

where Z_0 is the source or load resistance of the network analyzer (50 Ω), G_{peak} is the transmission gain in decibels at the peak of the measured frequency characteristic. The C_f branch refers to the feedthrough capacitance, through which the signal at the input port directly couples into the output port. The calculated lumped RLC values are summarized in Table 1.

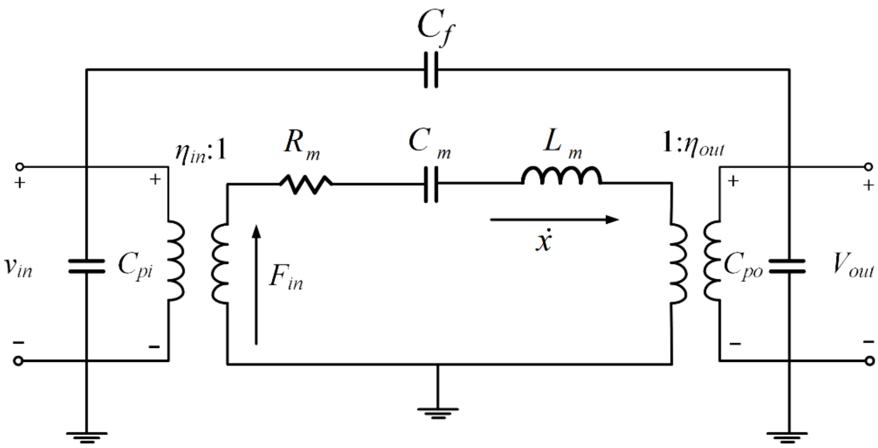

Figure 6. The equivalent circuit of the described resonator.

Table 1. Calculated lumped RLC values of various ΠBARs.

Type	Frequency (MHz)	R_m (MΩ)	L_m (H)	C_m (F)
A	26.7	1.0851	15.2291	2.3621×10^{-18}
B	20	0.7292	20.9852	3.0450×10^{-18}
C	26.7	2.0686	31.6398	1.1108×10^{-18}

Based on the equivalent model, the frequency responses were simulated and plotted in Figure 5 to provide a clear comparison with the measured responses. As can be seen, some discrepancies occurred, which can be attributed to the mode distortions induced by fabrication tolerances. As mentioned above, the mode distortions caused by warping contributed most to the Q degradations as well as asymmetrical peak shapes. Taking type B of 20 MHz, for example, by adjusting the parameters of the equivalent circuit model, a similar spectral curve with the experimental result was obtained. According to the equivalent circuit model, the equivalent stiffness and mass of the resonator can be expressed as follows [32]:

$$\begin{aligned} m_{eff} &= \eta^2 L_x \\ k_{eff} &= \frac{\eta^2}{C_x} \end{aligned} \tag{10}$$

As a result, the summary results of the calculated and fitted values based on the measured results of type B are shown in Table 2, showing that mode distortions contributed to the changes in equivalent mass and equivalent stiffness. For the simulated curves, there were anti-resonance frequencies associated with feedthrough signals, which were not observed in the measured ones. It can be inferred that the described fabrication process could effectively suppress the feedthroughs.

Table 2. The calculated and fitted RLC values of type B.

Parameters	The Calculated Results	The Fitted Results
R_m (MΩ)	0.7292	0.86160
L_m (H)	20.9852	18.0036
C_m (F)	3.0450×10^{-18}	4.002×10^{-18}
M_{eff} (kg)	1.1206×10^{-11}	9.6141×10^{-12}
k_{eff} (N/m)	1.7537×10^{5}	1.3344×10^{5}

The simulated Q_{anchor} values of three types of resonators were 5.75×10^7, 1.78×10^9, and 5.63×10^7, respectively, consistent with the tendencies of the measured values, which could provide helpful guidance for resonator optimization. However, all the measured Q values of the three types of resonators in air were moderate. Furthermore, the resonance peaks were not high enough. There could be several reasons for this. Firstly, the simulations assume ideal cases, however, there are in practice fabrication tolerances, material flaws, and process damage that are detrimental to Q values. Even so, the measured results were still far below the simulated ones. Noting that only the anchor loss was modeled, other loss mechanisms occurring should be considered. Air damping is generally a non-negligible loss source for MEMS resonators. As for other losses, thermoelastic damping (TED) is caused by irreversible heat flow [33–35], which results from the temperature gradients generated by the nonuniform stresses between different vibrating regions [36]. For BAW modes, with reduced volumetric differences during vibrations, TED is generally negligible. Akhiezer damping (AKE) is associated with irreversible phonon population relaxation [12,37]. When strain destroys the equilibrium of thermal phonons, the phonons tend to re-establish the thermal equilibrium through normal and Ümklapp processes; as a result irreversible phonon population relaxation occurs, the entropy increases and the energy is dissipated [10,38]. For low frequencies, around tens of MHz, AKE is generally overridden by other loss sources, which cannot be overcome. As for surface loss, this becomes notable for sub-micrometer resonators [39,40]. For ΠBARs with thickness of over 2 μm, this loss source is considered insignificant. To verify whether the air damping was overcome, the resonators were measured at high vacuum of 2×10^{-4} Torr.

The Q enhancements in vacuum were not significant, as expected. Taking type B as an example, as shown in Figure 7, the Q value increased from 3600 in air to 4941 in vacuum, corresponding to a 1.37-fold enhancement, which suggests that air damping could be ruled out as the dominant energy dissipation. The mode shape distortion resulting from the mechanical instability and fabrication tolerances may have contributed most to the Q degradations.

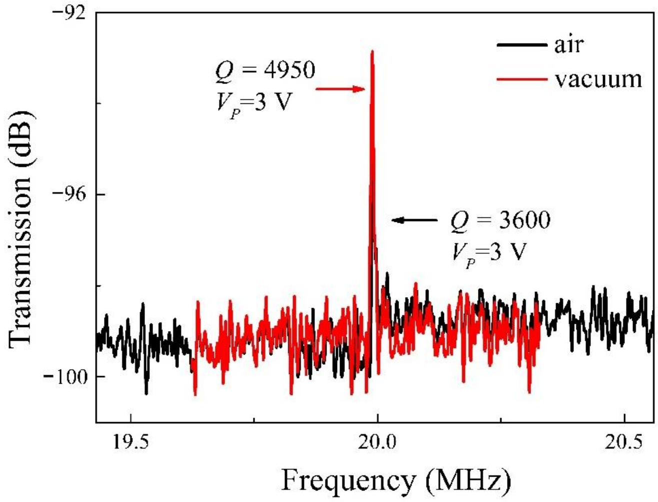

Figure 7. Comparison between the frequency spectra of type B ΠBAR with 20 MHz in air and vacuum.

3.2. Attributions of Moderate Q Values

Mechanical instability is detrimental to Q values. The vertical height profiles of the resonator were characterized using a 3D microscope. It was found that the resonator was warped downward, adopting an approximately symmetrical parabolic structure. As shown in Figure 8, the vertical height difference between the free end and the center of the coupling beam ranged from 0.4 µm to 0.5 µm. Therefore, significant out-of-plane vibrations were introduced which severely distorted the mode shape. Moreover, the overlapped transduction areas between the flange and the electrode were decreased. These two issues resulted in degraded Q values and limited resonance peaks. As shown in Figure 9, taking the 20 MHz ΠBAR as an example, the buckled resonator was simulated. The Q_{anchor} was calculated to be 88,908, which was four orders of magnitude lower than that of the stable case, consistent with the measured results. Due probably to the fabrication process-induced residual stress, the thin resonator was apt to warp, which distorted the mode shape, thus leading to severe energy dissipation. In the future, this problem is expected to be solved based on appropriate design and fabrication processes. Accordingly, SOI wafers with thicker device layers and lower intrinsic stresses can be adopted to alleviate this issue.

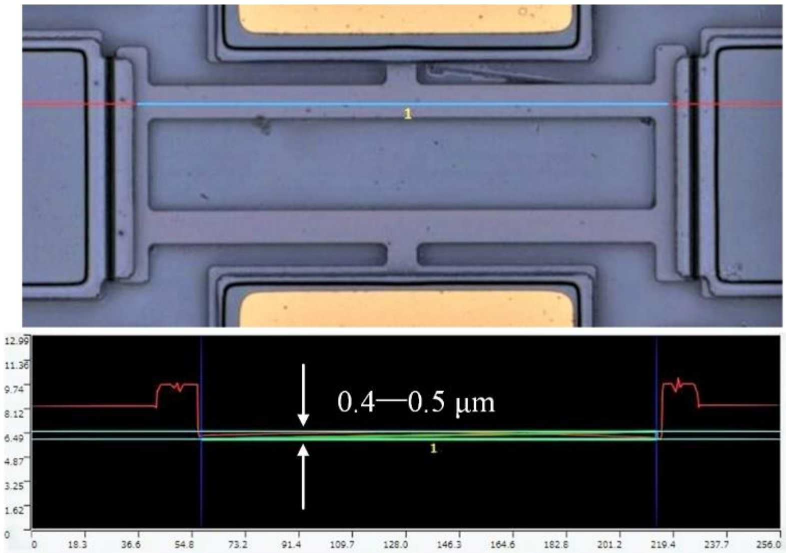

Figure 8. Warping occurred in ΠBAR by 3D microscope.

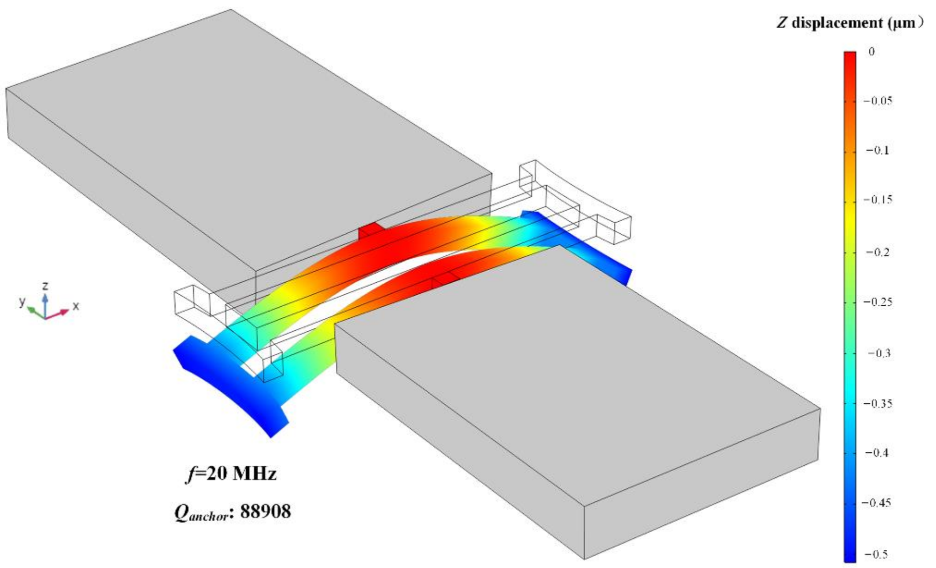

Figure 9. The simulated ΠBAR buckling and the calculated Q_{anchor}.

The Q values of resonators are susceptible to the fabrication process. With variations in tether dimensions, the actual displacement distribution substantially deviates from the optimally designed case. Therefore, Q_{anchor} values which are sensitive to the displacement distribution could be lowered. As shown in Figure 10, assuming the tether dimensions, L_s and W_s, vary within ± 2 μm around the optimal values for various ΠBARs, the Q_{anchor} values fluctuate sharply. As the ΠBAR is essentially a hybrid vibrating structure composed of straight beams and flanges of different shapes, the energy transfer among these mechanical components is relatively complicated, thus the displacement profiles are susceptible to geometric variations. With high dependence on the displacement distributions, the Q values could change dramatically. Taking type A, for example, as shown in Figure 10a, when the tether dimensions were exactly matched with the designed values, that is, $\Delta x = 0$, the simulated Q_{anchor} was 5.6×10^7. However, when the width of type A changed from 9.3 μm to 7.3 μm, the Q_{anchor} dramatically dropped from 5.6×10^7 to 1.9×10^7. Hence, process errors could also play an important role in Q degradations. Additionally, the variation tendencies of Q_{anchor} values for the various ΠBARs were different. Compared with B and C, type A suffered less from the tether dimension variations, which can be ascribed to its simple straight flanges and coupling beams. However, its measured Q value was inferior to that of type B because its designed Q value is inherently lower than that of type B. Nevertheless, by finding out the variation trends between the designed and fabricated geometrical parameters, compensation methods can be adopted during resonator design. Therefore, for tether B, despite its susceptibility to fabrication tolerances, its significant advantage of enlarged transduction areas remains; moreover, high Q values could still be expected with suitable compensation.

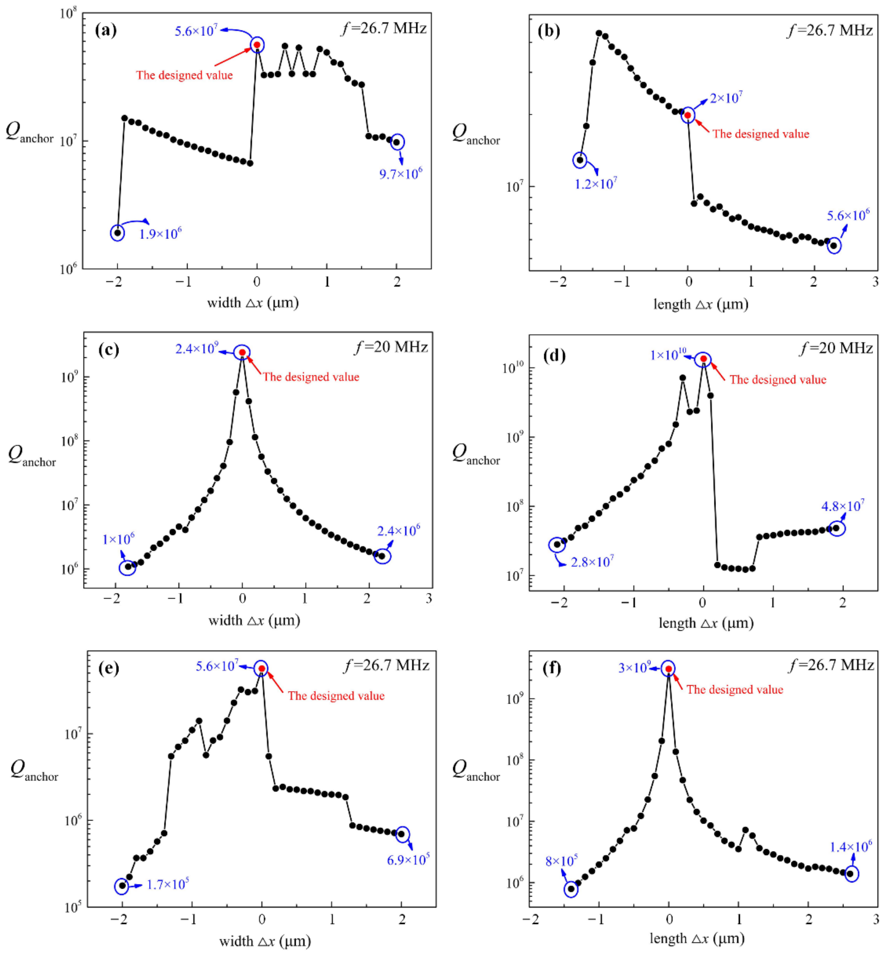

Figure 10. Calculated Q values versus tether width and length variations of ΠBARs of type A (**a**,**b**), type B (**c**,**d**), and type C (**e**,**f**).

In conclusion, although ΠBAR can be driven into vibrations with low bias voltages down to 3 V, which could have potential for building up high-performance timing reference devices with promising IC compatibility, there remain some shortcomings. Due to the mass loads at the two ends, the resonator is apt to warp, which distorts the mode shape, thus leading to severe energy dissipation. The device thickness should be increased, which creates a requirement for a high-aspect-ratio etching process. On the other hand, the Q of ΠBAR can be impaired by geometrical variations caused by fabrication tolerances. To avoid sharp Q reductions, appropriate geometrical ranges of the resonator in which Q varies moderately should be determined during the design stage. It should be noted that the currently existing shortcomings are expected to be solved based on appropriate design and fabrication processes.

4. Conclusions and Perspectives

In summary, a capacitively transduced ΠBAR was developed in this study. A comprehensive theoretical analysis, as well as systematical measurements, were undertaken.

Based on vibrational coupling length extensional mode, larger transduction areas and lower energy dissipations could be simultaneously implemented. For the first time, concave flanges with promising feasibility and flexibility were proposed, which enabled low bias voltages down to 3 V.

A simple and reliable SOI fabrication process was exploited for producing nanoscale spacing gaps, which greatly improved the electromechanical couplings.

The measured and simulated results have been clearly compared. Based on full analysis, strategies for improving the resonator performance and robustness have been provided.

In summary, high-performance ΠBARs could be viable candidates for constituting monolithic timing and frequency references which are highly desired in advanced electronic systems.

Author Contributions: Q.J. conducted the theoretical analysis and wrote the manuscript; Z.C. conceived and conducted the simulations; Q.J. and Z.C. fabricated the devices and conceived and conducted the experiments; W.L. and J.Y. validated and analyzed the experimental data; Y.Z. conceived the study, analyzed results and theoretical background; F.Y. principal investigator, coordinated the experiments. All authors reviewed the manuscript. All authors have read and agreed to the published version of the manuscript.

Funding: This research was funded by the National Key Research and Development Program of China (2018YFF01010300), the National Natural Science Foundation of China (61734007, 61804150), and the Key Research Program of Frontier Science of CAS (QYZDY-SSW-JSC004).

Institutional Review Board Statement: Not applicable.

Informed Consent Statement: Not applicable.

Conflicts of Interest: The authors declare no conflict of interest.

References

1. Basu, J.; Bhattacharyya, T.K. Microelectromechanical Resonators for Radio Frequency Communication Applications. *Microsyst. Technol.* **2011**, *17*, 1557–1580. [CrossRef]
2. Bahreyni, B. *Fabrication & Design of Resonant Microdevices*; William Andrew: New York, NY, USA, 2008.
3. Ng, E.; Yang, Y.; Hong, V.A.; Ahn, C.H.; Heinz, D.B.; Flader, I.; Chen, Y.; Everhart, C.L.M.; Kim, B.; Melamud, R.; et al. The long path from MEMS resonators to timing products. In Proceedings of the 28th IEEE International Conference on Micro Electro Mechanical Systems (MEMS), Estoril, Portugal, 18–22 January 2015; pp. 1–2.
4. Wang, T.; Chen, Z.; Jia, Q.; Yuan, Q.; Yang, J.; Yang, F. A Novel High Q Lamé-Mode Bulk Resonator with Low Bias Voltage. *Micromachines* **2020**, *11*, 737. [CrossRef] [PubMed]
5. Wu, G.; Xu, J.; Ng, E.J.; Chen, W. MEMS Resonators for Frequency Reference and Timing Applications. *J. Microelectromech. Syst.* **2020**, *29*, 1137–1166. [CrossRef]
6. Zhang, W.; Zhu, H.; Lee, J.E.Y. Piezoresistive transduction in a double-ended tuning fork SOI MEMS resonator for enhanced linear electrical performance. *IEEE Trans. Electron Devices* **2015**, *62*, 1596–1602. [CrossRef]

7. Zhu, H.; Tu, C.; Lee, J.E.Y.; Rufer, L. Active electronic cancellation of nonlinearity in a High-Q longitudinal-mode silicon resonator by current biasing. In Proceedings of the 2014 European Frequency and Time Forum (EFTF), Neuchâtel, Switzerland, 23–26 June 2014; pp. 12–15.
8. Wu, G.; Xu, J.; Zhang, X.; Wang, N.; Yan, D.; Lim, J.L.K.; Zhu, Y.; Li, W.; Gu, Y. Wafer-level vacuum-packaged high-performance AlN-on-SOI piezoelectric resonator for Sub-100-MHz oscillator applications. *IEEE Trans. Ind. Electron.* **2017**, *65*, 3576–3584. [CrossRef]
9. Chen, C.Y.; Li, M.H.; Li, S.S. CMOS-MEMS resonators and oscillators: A review. *Sens. Mater.* **2018**, *30*, 733–756.
10. Chandorkar, S.A.; Agarwal, M.; Melamud, R.; Candler, R.N.; Goodson, K.E.; Kenny, T.W. Limits of quality factor in bulk-mode micromechanical resonators. In Proceedings of the 2008 IEEE 21st International Conference on Micro Electro Mechanical Systems, Tucson, AZ, USA, 13–17 January 2008; pp. 74–77.
11. Vukasin, G.D.; Sanchez, V.K.; Glaze, J.; Bousse, N.E.; Bissel, N.; Shin, D.D.; Kwon, H.-K.; Heinz, D.; Yen, E.T.-T.; Kenny, T.W. Anchor Design Affects Dominant Energy Loss Mechanism in a Lamé Mode MEM Resonator. *J. Microelectromech. Syst.* **2020**, *29*, 860–866. [CrossRef]
12. Rodriguez, J.; Chandorkar, S.A.; Watson, C.A.; Glaze, G.M.; Ahn, C.H.; Ng, E.J.; Yang, Y.; Kenny, T.W. Direct detection of Akhiezer damping in a silicon MEMS resonator. *Sci. Rep.* **2019**, *9*, 2244. [CrossRef]
13. Daruwalla, A.; Wen, H.; Liu, C.S.; Ayazi, F. Low motional impedance distributed lamé mode resonators for high frequency timing applications. *Microsyst. Nanoeng.* **2020**, *6*, 53. [CrossRef]
14. Kaajakari, V.; Mattila, T.; Oja, A.; Kiihamaki, J.; Seppa, H. Square-extensional mode single-crystal silicon micromechanical resonator for low-phase-noise oscillator applications. *IEEE Electron Device Lett.* **2004**, *25*, 173–175. [CrossRef]
15. Khine, L.; Palaniapan, M.; Wong, W.K. 12.9 MHz Lamé-mode differential SOI bulk resonators. In Proceedings of the TRANSDUCERS 2007: International Solid-State Sensors, Actuators and Microsystems Conference, Lyon, France, 10–14 June 2007; pp. 1753–1756.
16. Ho, G.K.; Sundaresan, K.; Pourkamali, S.; Ayazi, F. Low-motional-impedance highly-tunable I/sup 2/resonators for temperature-compensated reference oscillators. In Proceedings of the 18th IEEE International Conference on Micro Electro Mechanical Systems (MEMS), Miami Beach, FL, USA, 30 January–3 February 2005; pp. 116–120.
17. Ho, G.K.; Sundaresan, K.; Pourkamali, S.; Ayazi, F. Micromechanical IBARs: Tunable high-*Q* resonators for temperature-compensated reference oscillators. *J. Microelectromech. Syst.* **2010**, *19*, 503–515. [CrossRef]
18. Sundaresan, K.; Ho, G.K.; Pourkamali, S.; Ayazi, F. A two-chip, 4-MHz, microelectromechanical reference oscillator. In Proceedings of the 2005 IEEE International Symposium on Circuits and Systems, Kobe, Japan, 23–26 May 2005; pp. 5461–5464.
19. Ho, G.K.K.; Sundaresan, K.; Pourkamali, S.; Ayazi, F. Temperature compensated IBAR reference oscillators. In Proceedings of the 19th IEEE International Conference on Micro Electro Mechanical Systems, Istanbul, Turkey, 22–26 January 2006; pp. 910–913.
20. Ho, G.K.; Perng, J.K.; Ayazi, F. Micromechanical IBARs: Modeling and process compensation. *J. Microelectromech. Syst.* **2010**, *19*, 516–525. [CrossRef]
21. Rahafrooz, A.; Pourkamali, S. Thermo-electro-mechanical modeling of high frequency thermally actuated I2-BAR resonators. In Proceedings of the Hilton Head 2010 Solid-State, Sensor, Actuator and Microsystems Workshop, 6 June 2010; pp. 74–77. Available online: https://www.semanticscholar.org/paper/THERMO-ELECTRO-MECHANICAL-MODELING-OF-HIGH-ACTUATED-Rahafrooz-Pourkamali/fd77c4f3f1299abdbff017dee1559c308f4bb8c6?sort=relevance (accessed on 13 March 2022). [CrossRef]
22. Wang, J.; Ren, Z.; Nguyen, C.C. 1.156-GHz self-aligned vibrating micromechanical disk resonator. *IEEE Trans. Ultrason. Ferroelectr. Freq. Control* **2004**, *51*, 1607–1628. [CrossRef] [PubMed]
23. Johnson, R.A. *Mechanical Filters. CRC Handbook of Electrical Filters*; CRC Press: Boca Raton, FL, USA, 2020; pp. 377–388.
24. Zhu, H.; Tu, C.; Lee, J.Y. Electronic tuning of Q and apparent TCf in a piezoresistive micromechanical resonator. In Proceedings of the 2013 IEEE 26th International Conference on Micro Electro Mechanical Systems (MEMS), Taipei, Taiwan, 20–24 January 2013; pp. 757–760.
25. Lee, J.E.Y.; Yan, J.; Seshia, A. A Low loss HF band SOI wine glass bulk mode capacitive square-plate resonator. *J. Micromech. Microeng.* **2009**, *19*, 074003. [CrossRef]
26. Yasumura, K.Y.; Stowe, T.D.; Chow, E.M.; Pfafman, T.; Kenny, T.W.; Stipe, B.C.; Rugar, D. Quality factors in micron-and submicron-thick cantilevers. *J. Microelectromech. Syst.* **2000**, *9*, 117–125. [CrossRef]
27. Darvishian, A.; Shiari, B.; Cho, J.Y.; Nagourney, T.; Najafi, K. Anchor loss in hemispherical shell resonators. *J. Microelectromech. Syst.* **2017**, *26*, 51–66. [CrossRef]
28. Tu, C.; Lee, J.E.Y.; Zhang, X.S. Dissipation Analysis Methods and Q-Enhancement Strategies in Piezoelectric MEMS Laterally Vibrating Resonators: A Review. *Sensors* **2020**, *20*, 4978. [CrossRef]
29. Uzunov, I.S.; Terzieva, M.D.; Nikolova, B.M.; Gaydazhiev, D.G. Extraction of modified butterworth—Van Dyke model of FBAR based on FEM analysis. In Proceedings of the 2017 XXVI International Scientific Conference Electronics (ET), Sozopol, Bulgaria, 13–15 September 2017.
30. Zhu, H. *Nonlinear Behavior and Temperature-Dependence of Frequency in Silicon Bulk-Mode Micromechanical Resonators*; City University of Hong Kong: Hong Kong, China, 2015.
31. Chen, Z.; Wang, T.; Jia, Q.; Yang, J.; Yuan, Q.; Zhu, Y.; Yang, F. A Novel Lamé Mode RF-MEMS Resonator with High Quality Factor. *Int. J. Mech. Sci.* **2021**, *204*, 106484. [CrossRef]

32. Colinet, E.; Arcamone, J.; Niel, A.; Lorent, E.; Hentz, S.; Ollier, E. 100 MHz oscillator based on a low polarization voltage capacitive Lamé-mode MEMS resonator. In Proceedings of the 2010 IEEE International Frequency Control Symposium, Newport Beach, CA, USA, 1–4 June 2010.
33. Pu, L.; Fang, Y.; Hu, R. Thermoelastic damping in rectangular and circular microplate resonators. *J. Sound Vib.* **2012**, *331*, 721–733.
34. Chen, Z.; Jia, Q.; Liu, W.; Yuan, Q.; Zhu, Y.; Yang, J.; Yang, F. Dominant Loss Mechanisms of Whispering Gallery Mode RF-MEMS Resonators with Wide Frequency Coverage. *Sensors* **2020**, *20*, 7017. [CrossRef]
35. Duwel, A.; Candler, R.N.; Kenny, T.W.; Varghese, M. Engineering MEMS resonators with low thermoelastic damping. *J. Microelectromech. Syst.* **2006**, *15*, 1437–1445. [CrossRef]
36. Lifshitz, R.; Roukes, M.L. Thermoelastic damping in micro-and nanomechanical systems. *Phys. Rev. B* **2000**, *61*, 5600. [CrossRef]
37. Kunal, K.; Aluru, N.R. Akhiezer damping in nanostructures. *Phys. Rev. B* **2011**, *84*, 245450. [CrossRef]
38. Ghaffari, S.; Chandorkar, S.A.; Wang, S.; Ng, E.J.; Ahn, C.H.; Hong, V.; Yang, Y.; Kenny, T.W. Quantum limit of quality factor in silicon micro and nano mechanical resonators. *Sci. Rep.* **2013**, *3*, 3244. [CrossRef] [PubMed]
39. Kim, B.; Hopcroft, M.A.; Candler, R.N.; Jha, C.M.; Agarwal, M.; Melamud, R.; Chandorkar, S.A.; Yama, G.; Kenny, T.W. Temperature dependence of quality factor in MEMS resonators. *J. Microelectromech. Syst.* **2008**, *17*, 755–766. [CrossRef]
40. Yang, J.; Ono, T.; Esashi, M. Dominated energy dissipation in ultrathin single crystal silicon cantilever: Surface loss. In Proceedings of the 13th Annual International Conference on Micro Electro Mechanical Systems (MEMS 2000), Miyazaki, Japan, 23–27 January 2000.